Detailed Heat Generation Simulations via the Monte Carlo Method

Eric Pop, Robert Dutton and Kenneth Goodson†

Department of Electrical (†and Mechanical) Engineering, Stanford University
Contact: epop@stanford.edu, Bldg 500 Room 501S, Stanford CA 94305-3030, tel 650.723.8482, fax 650.723.7657

***Abstract*— As current device technologies advance into the sub-continuum regime, they operate at length scales on the order of the electron and phonon mean free path. The ballistic conditions lead to strong non-equilibrium at nanometer length scales. The electron-phonon interaction is not energetically or spatially uniform and the generated phonons have widely varying contributions to heat transport. This work examines the microscopic details of Joule heating in bulk silicon with Monte Carlo simulations including acoustic and optical phonon dispersion. The approach provides an engineering tool for electro-thermal analysis of future nano-devices.**

I. INTRODUCTION

Understanding heat generation at nanometer scales in silicon is of great interest and particularly relevant to the heating and reliability of nanoscale and thin-film transistors. Joule heating is usually simulated as the dot product of the *macroscopic* electric field and current density [1]. This approach does not account for the *microscopic* non-locality of the phonon emission near a strongly peaked electric field region. It also does not differentiate between electron energy exchange with the various phonon modes and does not give any spectral information regarding the types of phonons emitted. The present work addresses both of these issues: we use a detailed Monte Carlo (MC) simulation to compute sub-continuum and phonon mode-specific heat generation rates, with applications at nanometer length scales.

In silicon, as in most semiconductors, high-field Joule heating is typically dominated by optical phonon emission. Optical phonons are slow and they make virtually no contribution to heat transport. Rather, they decay into the faster acoustic modes which carry the energy away from the hottest regions. Optical-acoustic decay times are relatively long (on the order of picoseconds [2]) compared to the electron-phonon scattering time (tenths of picoseconds). If the generation rate of optical modes due to Joule heating from current flow is higher than their rate of decay into acoustic modes, a phonon energy bottleneck is created and the optical mode density can build up over time, directly affecting electron transport. Fig. 1 shows a diagram of these energy transfer processes in silicon. The dashed lines symbolize the effect of phonons on the electron population and transport.

II. IMPLEMENTATION

This work uses the Monte Carlo method to compute the phonon generation rates in physical and momentum space

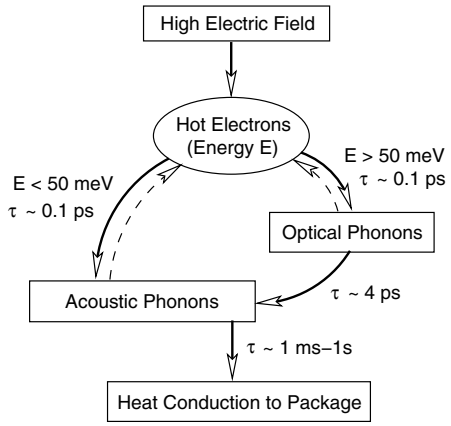

Fig. 1. Diagram and characteristic time scales of the energy transfer processes in silicon. Scattering with low group velocity optical phonons is the dominant relaxation mechanism for electron energies above 50 meV. This creates a phonon energy bottleneck until the optical phonons decay into the faster acoustic modes.

throughout the Brillouin zone. The electron energy bands are modeled analytically with non-parabolicity parameter $\alpha = 0.5$ eV^{-1} [3] and six ellipsoidal and energetically equivalent conduction band valleys. This is a good approximation for devices operating at voltages below the silicon bandgap (1.1 V), such as those of future technologies, and allows for significantly faster code that is easier to implement and debug. Full-band simulations [4], [5] have typically been used at higher voltages, when impact ionization and high energy transport play a larger role. This isn't the case for future low-power nanotechnologies, and consequently the present work limits the maximum electron energy to 1.1 eV during the simulation. Sub-bandgap impact ionization is also neglected.

As in the traditional analytic-band approach [3], inelastic scattering with six types of inter-valley phonons is incorporated. The inset of Fig. 2 illustrates the ellipsoidal conduction band valleys and the allowed phonon scattering transitions. Inter-valley scattering can be of g-type, when electrons scatter between valleys on the same axis, and of f-type when the scattering occurs between valleys on different axes [6]. Intra-valley scattering refers to scattering within the same conduction band valley and usually involves only acoustic phonons [7].

Many typical MC codes (as well as our earlier work [9]) treat intra-valley scattering with a single kind of acoustic

 0-7803-7826-1/03/$17.00 © 2003 IEEE

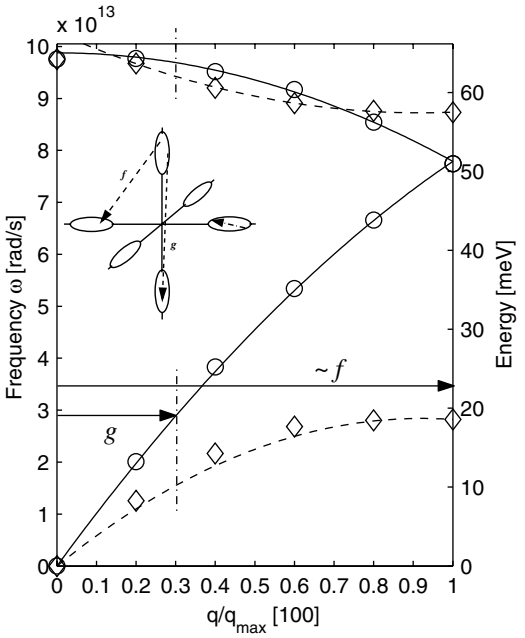

Fig. 2. Phonon dispersion relationship in silicon in the [100] direction, based on neutron scattering data (symbols) [8]. Circles and continuous lines mark longitudinal modes, diamonds and dashed lines mark transverse modes. The f and g phonons are involved in the inter-valley scattering of electrons [6].

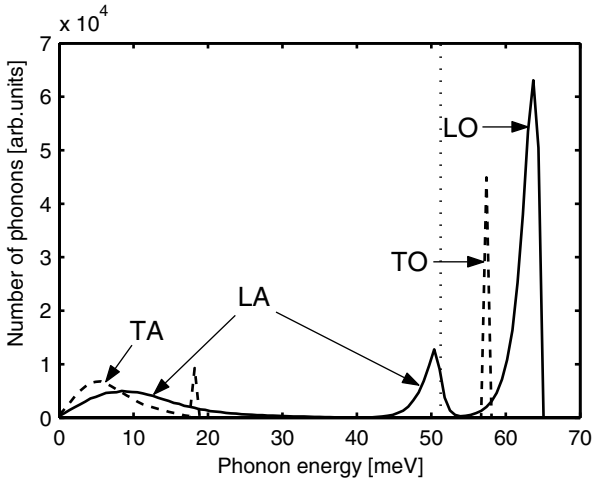

Fig. 3. Computed total phonon scattering spectrum (emission plus absorption) at a constant field of 40 kV/cm, as a function of phonon energy. The continuous line is for longitudinal phonons, dashed for transverse and the dotted vertical line marks the cutoff between the acoustic and optical modes, near 50 meV.

phonon by grouping the longitudinal acoustic (LA) and transverse acoustic (TA) branches into a dispersionless mode with a single velocity and a single deformation potential. Unlike the traditional approach, this work considers scattering with LA and TA modes separately. Each phonon dispersion branch from Fig. 2 is treated with the isotropic approximation

$$\omega_q = \omega_o + v_s q + c q^2 \tag{1}$$

where ω_q is the phonon frequency and q its wave vector. For the acoustic phonons, the parameters v_s and c are chosen to capture the slope of the dispersion near the Brillouin zone center and the maximum frequency at the zone edge [10]. The choice of parameters for longitudinal optical (LO) phonons insures that they meet the zone edge LA frequency. For both transverse acoustic and transverse optical (TO) phonons the zone edge slope (group velocity) is fit to zero. The continuous (longitudinal) and dashed (transverse) lines in Fig. 2 represent these quadratic approximations, and the fitting coefficients are listed in Table I. Quartic polynomials would offer a better fit in the [100] crystal direction but no advantage in the other directions, hence the quadratics are entirely sufficient for this isotropic approximation. They track the phonon dispersion data closely, especially in the regions relevant to electron-phonon scattering in silicon: near the Brillouin zone center for intra-valley acoustic phonons, and near the frequencies corresponding to inter-valley f- and g-type phonons. The quadratics are also easy to invert and, where needed, to extract the phonon wave vector as a function of its frequency.

TABLE I
QUADRATIC PHONON DISPERSION COEFFICIENTS.

	ω_o 10^{13} s^{-1}	v_s 10^5 cm/s	c 10^{-3} cm^2/s
LA	0.00	9.26	-2.22
TA	0.00	5.24	-2.28
LO	9.88	0.00	-1.60
TO	10.20	-2.57	1.12

The total intra-valley scattering rate is calculated separately with LA and TA phonons, as a function of the initial electron energy E_k:

$$\Gamma(E_k) = \frac{D_a^2 m^*}{4\pi\rho\hbar^2 k}\int_q \frac{1}{\omega_q}\left(N_q + \frac{1}{2} \mp \frac{1}{2}\right)\mathcal{I}_q^2 q^3 dq \tag{2}$$

where D_a is the respective deformation potential (LA or TA), m^* the electron density of states effective mass, ρ the mass density of silicon, k the electron wave vector in the spherical Herring-Vogt transformation [11], $N_q = 1/(\exp(\hbar\omega_q/k_bT) - 1)$ the phonon Bose-Einstein occupation number, and $\mathcal{I}_q$ the wave function overlap integral in the rigid ion approximation [12]. All quantities are numerically evaluated using the phonon dispersion from Eq. 1. The scattering rate integral is carried out over all phonon q that conserve both energy and momentum, as required by $|\cos(\phi)| \leq 1$, where

$$\cos(\phi) = \mp\frac{q}{2k} + \frac{m^*\omega_q}{\hbar k q}[1 + \alpha(2E_k \pm \hbar\omega_q)] \tag{3}$$

and ϕ is the angle between the phonon and initial electron wave vector. As in Eq. 2, the top and bottom signs refer to phonon absorption and emission, respectively. The intra-valley scattering rate typically cited in the literature [3] can be recovered by substituting $\omega_q = v_s q$ and $\mathcal{I}_q = 1$.

The LA and TA deformation potentials introduced in [11] as $D_{LA}(\theta) = \Xi_d + \Xi_u \cos^2\theta$ and $D_{TA}(\theta) = \Xi_u \sin\theta\cos\theta$ are isotropically averaged over all angles θ between the

0-7803-7826-1/03/$17.00 © 2003 IEEE

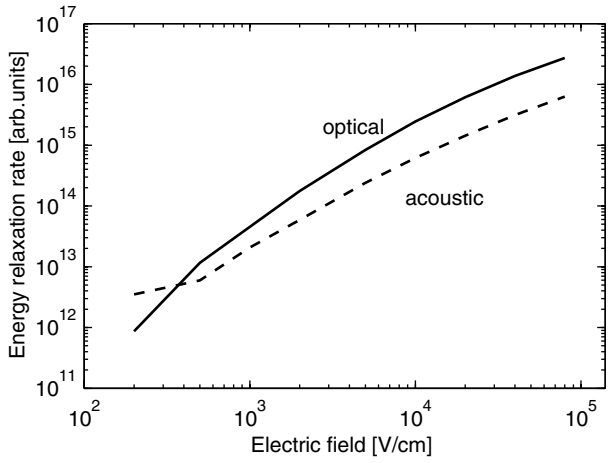

Fig. 4. Energy relaxation rates with optical and acoustic phonons as a function of applied steady-state electric field.

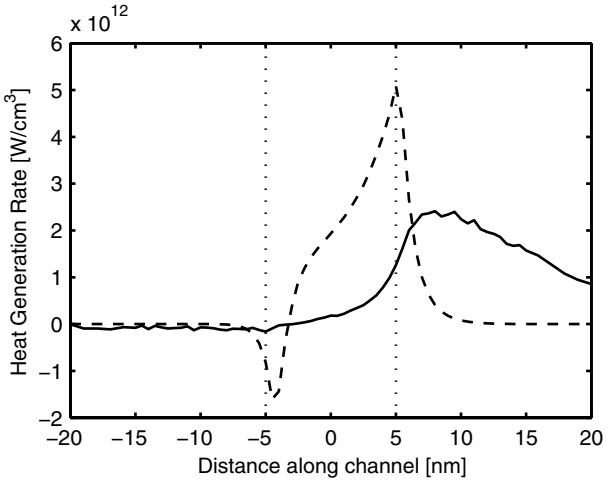

Fig. 5. Heat generation profile along the channel of a possible 10 nm transistor. The dashed line represents the heating rate obtained from the dot product of the electric field and the current, the solid line is the heating profile obtained with our MC simulations. The source and drain are to the left and right, respectively, of the vertical dotted lines.

phonon wave vector and the longitudinal axis of the conduction band valley. The values of the shear (Ξ_u) and dilation (Ξ_d) deformation potentials are chosen to match the low-field mobility data [13] at low temperatures (77 K), where acoustic scattering dominates. The angle-averaged LA and TA deformation potentials are found to be 6.4 eV and 3.1 eV respectively. To the best of our knowledge this is the first analytic-band MC work to distinguish between and include the dispersion of the two acoustic phonon polarizations. This becomes particularly relevant toward the edge of the Brillouin zone where transverse phonons are nearly stationary.

The phonon dispersion is also employed for inter-valley transitions involving the six f- and g-type acoustic and optical phonons (see Fig. 2). After the type of inter-valley scattering mechanism is determined, the final state of the electron is first chosen isotropically [3] and the phonon wave vector necessary for the transition can be calculated because the initial state of the electron is known. This is translated into a certain phonon energy using the phonon dispersion described above. The phonons that do not satisfy both energy and momentum conservation within a certain tolerance are discarded with a rejection algorithm. This is a relatively inexpensive search which ends when a suitable phonon is found.

The code implements all phonon scattering events as inelastic (whereas most traditional analytic-band, and even some full-band codes, often neglect energy relaxation with the acoustic modes) and electrons can exchange energy with phonons in arbitrarily small quantities. During the simulation all phonons absorbed and emitted are tallied, and full phonon generation statistics can be computed.

III. APPLICATIONS

Fig. 3 shows the total computed phonon scattering statistics (for both intra- and inter-valley scattering) in a steady state field of 40 kV/cm. Note the cutoff energy of the various phonon branches as required by their respective dispersion relation from Fig. 2. Few acoustic phonons are generated at the lowest energies because their density of states vanishes near the Brillouin zone center. Intra-valley scattering also decreases at higher energies as fewer electrons with large enough energy and/or momentum are available to interact with those phonons. The sharp peaks occur due to strong Umklapp inter-valley scattering with phonons of $q = 0.3q_{max}$ (g-type) and those near the edge of the Brillouin zone (f-type) as referred to in Fig. 2 and [6]. The relative magnitude of the peaks depends on the choice of inter-valley deformation potentials. This work uses those from [3], which are the ones most often cited in the literature, although they are not unique [13].

Fig. 4 compares the net (emission minus absorption) acoustic and optical phonon generation rates for various steady-state electric fields. Inter-valley optical phonon emission dominates at all but the lowest fields, where the average electrons are not yet hot enough to generate optical phonons, whose cut-off energy is near 50 meV.

The simulation can also be run in the context of a real electronic device, by importing a 1- or 2-dimensional electric field grid from another device simulator. The detailed phonon generation rates (in both real and momentum space) are then computed with MC runs in this "frozen-field" approximation and information can be extracted to aid in the thermal design of future generations of nanotransistors. This is particularly important in the sub-continuum limit, i.e. at dimensions comparable to or less than the electron and phonon mean free path (on the order of 5 and 100 nm in silicon devices, respectively). Fig. 5 shows the simulated heat generation profile in the 10 nm device proposed by [14] using a voltage $V_{dd} = 0.6$ V. The discrepancy between the macroscopic ($\mathbf{J} \cdot \mathbf{E}$) and MC heat generation profile is clear at such small scales. Electrons are injected almost ballistically across the short channel and begin releasing their energy to the lattice just inside the drain. The peak heating rate predicted by MC occurs a few nanometers

0-7803-7826-1/03/$17.00 © 2003 IEEE

into the drain, downstream from the macroscopic prediction, as electrons travel a few more mean free paths beyond the peak electric field. The shape of the MC heating rate is also different: electrons lose energy more gradually (about 50-60 meV, or one optical phonon per scattering length) than the classical prediction, where the electric field drops to zero inside the highly doped drain. The MC heat generation model is essential for predicting the mixture of electrons and phonons inside the drain "hot spot," which can be used as an input to a phonon Boltzmann Transport Equation (BTE) solver. Ballistic phonon emission from the drain hot spot may affect the source-side electron injection [15] and therefore limit the ultimate current drive of such short devices.

IV. CONCLUSIONS

This work represents a simulation approach which fills the gap of engineering tools between simple analytic-band MC codes [3] and more complex full-band simulators [4], [5]. The emphasis is on sophisticated physical modeling within a computationally efficient framework. The use of analytical electron bands and phonon dispersion enables simulations which are orders of magnitude faster than full-band techniques, and very accessible on modern desktop computers. This method has direct applications to the engineering of nano-devices and materials that require detailed knowledge of the heat generation spectrum.

Ongoing work is exploring the extension of these simulations to confined (and quantized) 2-dimensional electron and phonon systems (e.g. ultra-thin films) and to coupled electro-thermal simulations that feed the generated phonon densities back into the electron MC calculation. The information, documentation, and source code will be shared online [16].

ACKNOWLEDGMENT

The authors wish to thank Massimo Fischetti, Christoph Jungemann and Steve Laux for many valuable discussions. E. Pop is supported by the SRC-IBM graduate fellowship.

REFERENCES

[1] P. Sverdrup, Y. S. Ju, and K. E. Goodson, "Sub-continuum simulations of heat conduction in silicon-on-insulator transistors," *Journal of Heat Transfer*, vol. 123, pp. 130–137, 2001.

[2] D. K. Ferry, *Semiconductor transport*. Taylor & Francis, 2000.

[3] C. Jacoboni and L. Reggiani, "The Monte Carlo method for the solution of charge transport in semiconductor with applications to covalent materials," *Reviews of Modern Physics*, vol. 55, no. 3, pp. 645–705, July 1983.

[4] M. V. Fischetti and S. E. Laux, "Monte Carlo analysis of electron transport in small semiconductor devices including band-structure and space-charge effects," *Physical Review B*, vol. 38, no. 14, pp. 9721–9745, 1988.

[5] T. Kunikiyo, M. Takenaka, Y. Kamakura, M. Yamaji, H. Mizuno, M. Morifuji, K. Taniguchi, and C. Hamaguchi, "A Monte Carlo simulation of anisotropic electron transport in silicon including full band structure and anisotropic impact-ionization model," *Journal of Applied Physics*, vol. 75, no. 1, pp. 297–312, 1994.

[6] D. Long, "Scattering of conduction electrons by lattice vibrations in silicon," *Physical Review*, vol. 120, no. 6, pp. 2024–2032, 1960.

[7] C. Hamaguchi, *Basic semiconductor physics*. Springer, 2001.

[8] G. Dolling, "Lattice vibrations in crystals with the diamond structure," in *Symposium on Inelastic Scattering of Neutrons in Solids and Liquids*, Sept. 1963, pp. 37–48.

[9] E. Pop, S. Sinha, and K. E. Goodson, "Monte Carlo modeling of heat generation in electronic nanostructures," in *Proc. International Mechanical Engineering Congress and Expo (IMECE)*, Nov. 2002.

[10] B. Fischer and K. R. Hofmann, "A full-band Monte Carlo model for the temperature dependence of electron and hole transport in silicon," *Applied Physics Letters*, vol. 76, no. 5, pp. 583–585, 2000.

[11] C. Herring and E. Vogt, "Transport and deformation-potential theory for many-valley semiconductors with anisotropic scattering," *Physical Review*, vol. 101, no. 3, pp. 944–961, 1956.

[12] A. Haug, *Theoretical solid state physics*. Pergamon Press, 1972, vol. 2.

[13] C. Canali, C. Jacoboni, F. Nava, G. Ottaviani, and A. Alberigi-Quaranta, "Electron drift velocity in silicon," *Physical Review B*, vol. 12, no. 4, pp. 2265–2284, 1975.

[14] M. Lundstrom and Z. Ren, "Essential physics of carrier transport in nanoscale MOSFETs," *IEEE Trans. Electron Devices*, vol. 49, pp. 133–141, 2002.

[15] E. Pop, K. Banerjee, P. Sverdrup, R. Dutton, and K. E. Goodson, "Localized heating effects and scaling of sub-0.18 micron CMOS devices," in *Proc. IEEE International Electron Devices Meeting (IEDM)*, Dec. 2001, pp. 677–680.

[16] Monet. [Online]. Available: http://nanoheat.stanford.edu